

Design of flexible multi-mode fiber endoscope

Ruo Yu Gu,¹ Reza Nasiri Mahalati,^{1,2} and Joseph M. Kahn^{1,*}

¹*E. L. Ginzton Laboratory and Department of Electrical Engineering Stanford University, Stanford, California 94305, USA*

²*Apple Inc., Cupertino, California 95014, USA*
jmk@ee.stanford.edu

Abstract: Multi-mode fiber (MMF) endoscopes are extremely thin and have higher spatial resolution than conventional endoscopes; however, all current MMF endoscope designs require either that the MMF remain rigid during insertion and imaging or that the orientation of the MMF be known. This limits their possible medical applications. We describe an MMF endoscope design that allows the MMF to be arbitrarily bent as it is maneuvered to the target site prior to imaging. This is achieved by the addition of a partial reflector to the distal end of the MMF, which allows measurement of the mode coupling in the MMF using the reflected light arriving at the proximal end of the MMF. This measurement can be performed while the distal end of the endoscope is not directly accessible, as when the endoscope is being maneuvered. We simulate imaging through such a flexible MMF endoscope, where the MMF is step-index with 1588 spatial modes, and obtain an image even after the mode coupling matrix of the MMF is altered randomly, corresponding to an unknown bending of the MMF.

©2015 Optical Society of America

OCIS codes: (060.2350) Fiber optics imaging; (100.3010) Image reconstruction techniques; (170.2150) Endoscopic imaging.

References and links

1. B. A. Flusberg, E. D. Cocker, W. Piyawattanametha, J. C. Jung, E. L. M. Cheung, and M. J. Schnitzer, "Fiber-optic fluorescence imaging," *Nat. Methods* **2**(12), 941–950 (2005).
2. R. N. Mahalati, R. Y. Gu, and J. M. Kahn, "Resolution limits for imaging through multi-mode fiber," *Opt. Express* **21**(2), 1656–1668 (2013).
3. T. F. Massoud, Y. Murayama, F. Viñuela, and A. Utsumi, "Laboratory evaluation of a microangioscope for potential percutaneous cerebrovascular applications," *AJNR Am. J. Neuroradiol.* **22**(2), 363–365 (2001).
4. M. Plöschner, B. Straka, K. Dholakia, and T. Čížmár, "GPU accelerated toolbox for real-time beam-shaping in multimode fibres," *Opt. Express* **22**(3), 2933–2947 (2014).
5. A. M. Caravaca-Aguirre, E. Niv, and R. Piestun, "High-speed phase modulation for multimode fiber endoscope," *Imaging Appl. Opt.* (2014).
6. R. Y. Gu, R. N. Mahalati, and J. M. Kahn, "Noise-reduction algorithms for optimization-based imaging through multi-mode fiber," *Opt. Express* **22**(12), 15118–15132 (2014).
7. D. Loterie, S. Farahi, I. Papadopoulos, A. Goy, D. Psaltis, and C. Moser, "Digital confocal microscopy through a multimode fiber," <http://arxiv.org/abs/1502.04172> (2015).
8. Y. Choi, P. Hosseini, W. Choi, R. R. Dasari, P. T. C. So, and Z. Yaqoob, "Dynamic speckle illumination wide-field reflection phase microscopy," *Opt. Lett.* **39**(20), 6062–6065 (2014).
9. E. E. Morales-Delgado, S. Farahi, I. N. Papadopoulos, D. Psaltis, and C. Moser, "Delivery of focused short pulses through a multimode fiber," *Opt. Express* **23**(7), 9109–9120 (2015).
10. Y. Choi, C. Yoon, M. Kim, W. Choi, and W. Choi, "Optical imaging with the use of a scattering lens," *IEEE J. Sel. Top. Quantum Electron.* **20**(2), 61–73 (2014).
11. S. Bianchi, V. P. Rajamanickam, L. Ferrara, E. Di Fabrizio, R. Di Leonardo, and C. Liberale, "High numerical aperture imaging by using multimode fibers with micro-fabricated optics," in *CLEO: Science and Innovations* (OSA, 2014), paper SM2N.6.
12. M. Plöschner and T. Čížmár, "Compact multimode fiber beam-shaping system based on GPU accelerated digital holography," *Opt. Lett.* **40**(2), 197–200 (2015).
13. Y. Pu, X. Yang, I. Papadopoulos, S. Farahi, C. Hsieh, C. A. Ong, D. Psaltis, C. Moser, D. Psaltis, and K. M. Stankovic, "Imaging of the mouse cochlea with two-photon microscopy and multimode fiber-based microendoscopy," in *Biomedical Optics* (OSA, 2014), paper BT4A.3.

14. A. M. Caravaca Aguirre and R. Piestun, "Robustness of multimode fiber focusing through wavefront shaping," in *Latin America Optics and Photonics Conference* (2014).
15. S. Farahi, D. Ziegler, I. N. Papadopoulos, D. Psaltis, and C. Moser, "Dynamic bending compensation while focusing through a multimode fiber," *Opt. Express* **21**(19), 22504–22514 (2013).
16. M. Plöschner, T. Tyc, and T. Čižmár, "Seeing through chaos in multimode fibres," *Nat. Photonics* **9**(8), 529–535 (2015).
17. G. P. Agrawal, *Nonlinear Fiber Optics* (Academic, 2007).
18. D. Marcuse, *Theory of Dielectric Optical Waveguides*, 2nd ed. (Academic, 1991).
19. H. A. Haus, *Waves and Fields in Optoelectronics*, 3rd ed. (Prentice-Hall, 1984).
20. A. W. Snyder and J. D. Love, *Optical Waveguide Theory* (Springer Science & Business Media, 1983).
21. R. A. Panicker and J. M. Kahn, "Algorithms for compensation of multimode fiber dispersion using adaptive optics," *J. Lightwave Technol.* **27**(24), 5790–5799 (2009).
22. T. F. Massoud, "Method and device for treating intracranial vascular aneurysms," U.S. Patent 5,776,097 (1998).
23. R. A. Horn, *Matrix Analysis*, 2nd ed. (Cambridge University, 2013).
24. M. Sasaki, T. Ando, S. Nogawa, and K. Hane, "Direct photolithography on optical fiber end," *Jpn. J. Appl. Phys.* **41**(Part 1, No. 6B), 4350–4355 (2002).
25. J. Mertz, *Introduction to Optical Microscopy* (Roberts and Co. Publishers, 2010).
26. A. Edelman and N. R. Rao, "Random matrix theory," *Acta Numer.* **14**, 233–297 (2005).
27. T. Čižmár and K. Dholakia, "Exploiting multimode waveguides for pure fibre-based imaging," *Nat. Commun.* **3**, 1027 (2012).

1. Introduction

Multi-mode fiber (MMF) endoscopes are a class of endoscope that can be made much thinner than endoscopes of other designs [1], while maintaining a high resolution [2], opening up new medical applications [3]. Recent improvements in imaging speed [4,5] and signal-to-noise ratio (SNR) [6,7], as well as numerous other developments [8–12], bring these endoscopes closer to being practical medical devices, and biological imaging has been demonstrated in several experiments [7,10,13]. All MMF endoscopes require a calibration procedure to measure the mode coupling in the MMF before they can be used for imaging. This calibration requires placing an apparatus of substantial size at the distal end of the endoscope. Any bending of the MMF after calibration will adversely affect the calibration accuracy, thus degrading any images that are recorded through the endoscope [14,15]. Hence, a major drawback of MMF endoscopes is that the MMF must be held rigid at all times during calibration, insertion and imaging; or else that the orientation of the MMF be precisely known [16].

In this paper, we propose a design for an MMF endoscope that can be bent arbitrarily while it is maneuvered to the imaging site. This is achieved by attaching a partial reflector to the distal end of the MMF, which reflects light back to the proximal end of the MMF, allowing calibration of the MMF endoscope to be performed. The MMF endoscope can thus be calibrated after any bending occurs, ensuring accuracy during subsequent imaging. We describe this calibration procedure in detail in this paper. In Section 2, we describe forward and backward light propagation through the MMF. In Section 3, we describe how calibration is performed, both with and without access to the distal end of the MMF. In Section 4, we describe how imaging is performed once the MMF is calibrated. In Section 5, we present simulations of imaging through the apparatus using the procedures described. We discuss the results in Section 6, and provide conclusions in Section 7.

2. Propagation of light through MMF

In this section, we briefly describe a model for light propagation through an MMF to serve as a basis for subsequent sections. We assume that all light is continuous-wave (CW) and single-wavelength; the latter is a valid approximation of laser output as the properties of the MMF are constant over the typical laser linewidths available (under 1 fm). The CW assumption means that fiber dispersion and any transient time effects can be ignored. We expect the laser power to be sufficiently small that we can ignore any nonlinear effects in the MMF [17].

All light propagating between the proximal and distal ends of the MMF can be decomposed into a set of orthogonal guided modes. We refer to the direction from proximal to

distal as “forward” and the opposite direction as “backward”. At every point along the MMF we orient a local right-handed Cartesian coordinate system (x, y, z) whose $+z$ axis is a tangent to the central axis of the fiber and points in the forward direction. As orthogonal modes, we choose the local normal modes of the MMF [18]. At each (x, y, z) , these are mathematically equivalent to the ideal TE, TM, HE and EH modes of a straight fiber with the same coordinate system. The $\vec{\mathbf{E}}(x, y, z, t)$ and $\vec{\mathbf{H}}(x, y, z, t)$ fields of the modes are described in [18], and equivalently described using phasor notation as complex $\vec{\mathbf{E}}(x, y, z)$ and $\vec{\mathbf{H}}(x, y, z)$. There are an equal number of backward-propagating modes which have fields $\vec{\mathbf{E}}^*(x, y, z)$ and $-\vec{\mathbf{H}}^*(x, y, z)$, where the asterisk represents the complex conjugate. Note that all modes are normalized to have unit power. The amplitude and phase of each mode at any location in the MMF is then described by a single complex coefficient, and the amplitude, phase and polarization of the electric and magnetic fields inside the MMF are thus completely described by a single complex $2N \times 1$ vector, where N is the number of forward-propagating modes.

As the modes propagate through the MMF, imperfections in the MMF and macro-bends of the MMF cause some propagating modes to couple into other propagating modes and radiative modes, the latter causing loss. The relations between all modes can be described using scattering-matrix theory [19], as described in Eq. (1) and shown in Fig. 1.



Fig. 1. System diagram of a hypothetical MMF with three forward- and three backward-propagating modes. Forward- and backward-propagating modes are represented by arrows pointed to the right and left, respectively. The complex amplitudes of these modes, \mathbf{a} and \mathbf{b} , are measured at both the proximal and distal facets of the MMF. The matrix (\mathbf{S}) represents coupling between the modes.

$$\mathbf{b} = \mathbf{S}\mathbf{a}$$

$$\begin{bmatrix} \mathbf{b}_p \\ \mathbf{b}_d \end{bmatrix} = \begin{bmatrix} \mathbf{S}_{pp} & \mathbf{S}_{pd} \\ \mathbf{S}_{dp} & \mathbf{S}_{dd} \end{bmatrix} \begin{bmatrix} \mathbf{a}_p \\ \mathbf{a}_d \end{bmatrix} \quad (1)$$

In Eq. (1), $\mathbf{a} = [\mathbf{a}_p^T \quad \mathbf{a}_d^T]^T$ is the $2N \times 1$ vector of the coefficients of all modes entering the MMF (from either end), $\mathbf{b} = [\mathbf{b}_p^T \quad \mathbf{b}_d^T]^T$ is the $2N \times 1$ vector of the coefficients of all modes exiting the MMF, and \mathbf{S} is a $2N \times 2N$ matrix that describes the relation between the coefficients (for one MMF orientation). The subscripts p and d stand for proximal and distal, respectively. Since an MMF of approximately 1-2 meters in length has negligible loss [20], the system can be considered to obey conservation of power and hence:

$$\mathbf{S}^{-1} = \mathbf{S}^\dagger, \quad (2)$$

where the dagger represents the conjugate transpose. We assume that the MMF has symmetric dielectric and magnetic tensors in both the core and cladding, so the system obeys reciprocity, meaning that:

$$\mathbf{S}^T = \mathbf{S}. \quad (3)$$

In particular, this means that $\mathbf{S}_{pd} = \mathbf{S}_{dp}^T$. We assume that forward-propagating modes do not couple into backward-propagating modes, which means that $\mathbf{S}_{pp} = \mathbf{S}_{dd} = \mathbf{0}$. This allows Eq. (1) to be decoupled into two equations, such that if light enters the proximal end, the light at the distal end is described by:

$$\mathbf{b}_d = \mathbf{U}\mathbf{a}_p, \quad (4)$$

where we have denoted \mathbf{S}_{dp} by a matrix \mathbf{U} to simplify notation. Conversely, if light enters the distal end, the light at the proximal end is given by:

$$\mathbf{b}_p = \mathbf{U}^T\mathbf{a}_d. \quad (5)$$

From Eq. (2), we deduce that \mathbf{U} is unitary. As a convention, in the remainder of this paper, we will use \mathbf{a} to describe the coefficients of modes entering the MMF and \mathbf{b} to describe the coefficients of modes exiting the MMF.

3. Endoscope apparatus and calibration procedures

3.1 Endoscope apparatus

The apparatus of the flexible MMF endoscope is shown in Fig. 2. The configuration for fiber calibration at the distal end is shown in Fig. 2(a), and the configuration for fiber calibration at the proximal end and subsequent imaging is shown in Fig. 2(b). Common components in both configurations are a single-longitudinal-mode laser (a wavelength of 532 nm is assumed), a polarization-maintaining single mode fiber (PMF), a polarizing beamsplitter (PBS), a half-wave plate (HWP), and a phase-only spatial light modulator (SLM), which are together used to excite an arbitrary superposition of modes in an MMF. To avoid the zero diffraction order, a phase ramp on the SLM steers the first order into the MMF core. The phase-only SLM performs both phase and amplitude modulation by using high-frequency phase patterns to scatter light into other orders, which are blocked by the limited numerical aperture (NA) of the MMF and other components [21]. The remaining components in Fig. 2(a) measure the electric field at the distal end of the MMF, while those in Fig. 2(b) measure the forward- and backward-propagating electric fields at the proximal end of the MMF. An optical isolator prevents unwanted reflections back to the laser and SLM. Beam stop S1 is used to control the reference beam so that coherent measurements of both amplitude and phase can be made, and beam stops S2 and S3 are used in Fig. 2(b) to block the backward- and forward-propagating beams at the proximal end of the MMF, respectively. Beam stop S4 is used to block light reflecting from the object during calibration from the proximal end, and is open during calibration from the distal end (as shown in Fig. 2(a)) and during imaging (as shown in Fig. 2(b)). The polarizing beam displacer (PBD) is used for simultaneous measurement of both polarizations on the camera. All components remain in place when changing from Fig. 2(a) to Fig. 2(b), except for that lens L5 and the distal-end mirror are removed.

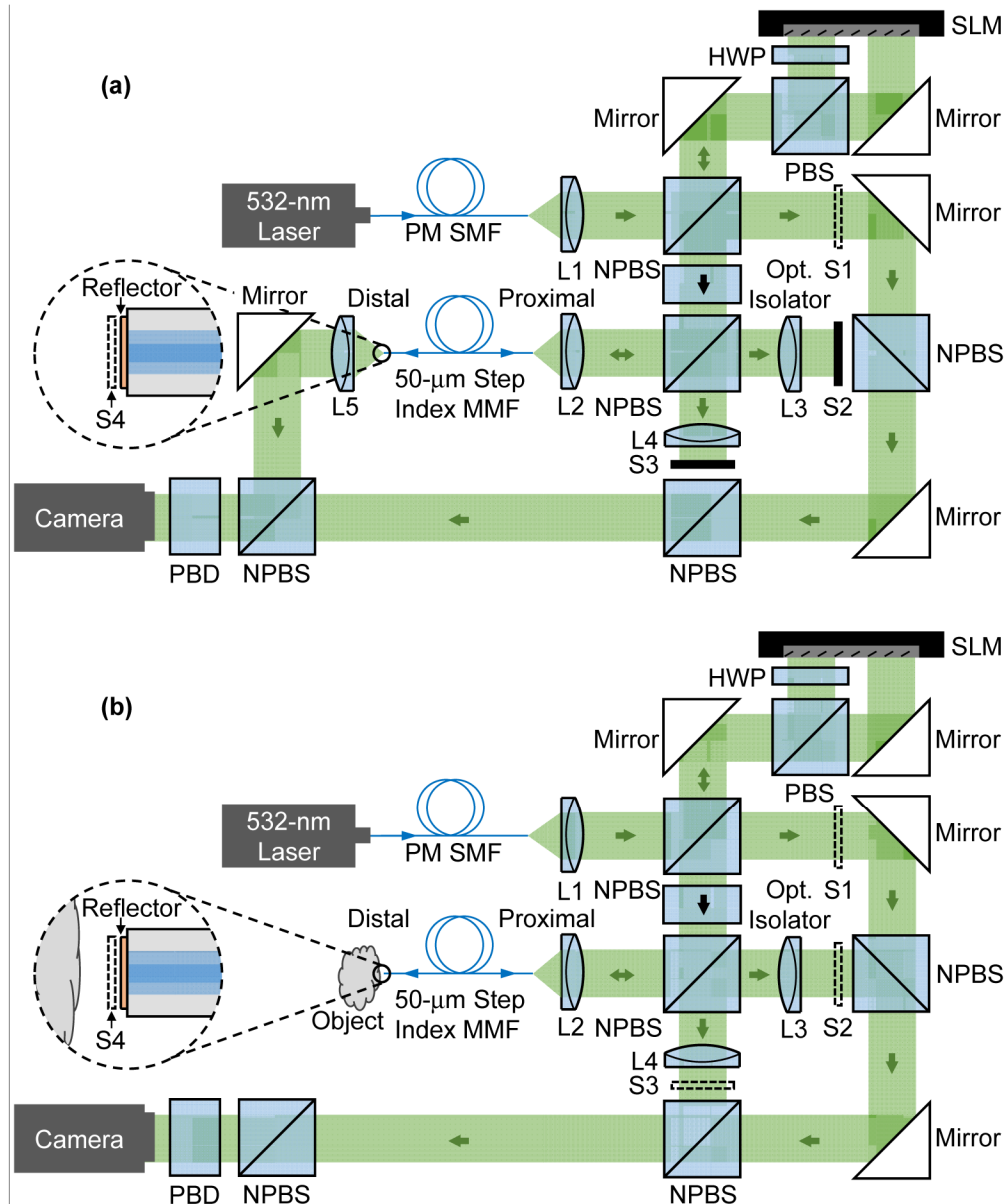


Fig. 2. MMF endoscope apparatus for (a) distal calibration and (b) proximal calibration and imaging. In (a), the electric field at the distal end of the MMF is measured, and in (b) the electric field at the proximal end of the MMF is measured. As explained in the text, beam stop S1 is used to obtain a coherent measurement of the electric field; beam stops S2 and S3 are used to isolate different beams incident on the camera, and beam stop S4 is used to block light reflecting from the object during proximal calibration.

The MMF is assumed to have an NA of 0.19 and a core diameter of 50 μm, which corresponds to $N = 1588$ forward-propagating modes (including spatial and polarization degrees of freedom). The proximal facet is AR-coated. The distal facet is equipped with a thin partial reflector, which partially reflects light reaching the distal end, and which is patterned so that its reflectance varies across the MMF core. For proximal calibration to be possible, this pattern must satisfy a set of constraints. These constraints are specified in detail below,

and a specific example of the partial reflector design is provided in Section 3. It should be noted that there is significant freedom in choosing the properties of the reflector, including its reflectance values and the dimensions in the pattern.

Mathematically, the endoscope apparatus can be described using Eqs. (6) and (7). From the proximal end to the distal end, the transmission path through the endoscope consists of the MMF and reflector, and is described by:

$$\mathbf{b} = \mathbf{T}\mathbf{U}\mathbf{a}, \quad (6)$$

where \mathbf{a} is a $N \times 1$ vector of the coefficients of modes entering the MMF, \mathbf{b} is a $2P \times 1$ vector representing an $\vec{\mathbf{E}}(x, y)$ field sampled in the x - and y -polarizations on a two-dimensional mesh containing P points (the ordering is arbitrary but must be consistent), and \mathbf{T} is a $2P \times N$ matrix whose columns are the electric fields of each mode after transmission through the reflector, just outside the MMF. Any field components in the z -polarization are not measured. Note that \mathbf{b} cannot be expressed as a superposition of the modes of \mathbf{a} , since there is no guarantee that these modes span all possible electric fields after transmission through the reflector. From the proximal end back to the proximal end, the reflection path through the endoscope consists of the MMF, the reflector, and the MMF again, and is described by:

$$\mathbf{b} = \mathbf{U}^T \mathbf{R} \mathbf{U} \mathbf{a}, \quad (7)$$

where \mathbf{a} and \mathbf{b} are the $N \times 1$ vectors of the coefficients of modes entering and exiting the MMF respectively, and \mathbf{R} is a $N \times N$ matrix describing the reflectance of every mode at the reflector, including mode coupling. To obtain Eq. (7) we have combined Eqs. (4) and (5) from Section 2.

3.2 Distal calibration procedure

To be able to excite a specific superposition of modes at the distal end of the MMF, as required for imaging, it is necessary to measure the matrix \mathbf{U} , and to image through a flexible MMF, \mathbf{U} must be measured while only the proximal end is accessible. We shall show that this is possible, with three caveats. First, it is necessary to have a rough approximation of \mathbf{U} in order to measure \mathbf{U} accurately. Thus, a measurement of \mathbf{U} from the distal end must first be performed prior to any imaging, as in rigid-MMF endoscopy. Subsequently, whenever the MMF is perturbed (bent), measurements of \mathbf{U} can be made from the proximal end using the prior measurement as an approximation, and each measurement provides an approximation for the subsequent measurement. The error that can be tolerated in the approximation or, alternatively, the amount of perturbation allowed, is significant, and will be characterized in more detail below. Second, the calibration measurements must not be affected by light entering from the distal end of the MMF. Thus, a shutter (beam stop S4) is placed at the distal end of the MMF to ensure that light is excluded during calibration but not imaging. The requirement for this shutter is compatible with applications where the endoscope is inside a thin cylindrical structure, such as in angioscopy [22], but may not be compatible with applications where the MMF must be sheathed inside a very thin needle. Third, the transmittance \mathbf{T} and reflectance \mathbf{R} of the reflector must be known and must remain constant during calibration and imaging. Ideally, these should be measured during endoscope fabrication; they can be measured accurately as long as \mathbf{U} is known, as seen in Eqs. (6) and (7). A possible procedure for measuring \mathbf{T} and \mathbf{R} is to measure \mathbf{U} before the reflector is attached, attach the reflector while keeping the MMF unperturbed, and then measure the transmitted and reflected light to determine \mathbf{T} and \mathbf{R} using Eqs. (6) and (7).

The calibration procedure is now described. First, distal calibration is performed while the distal end of the MMF is accessible. The apparatus is configured as in Fig. 2(a) and \mathbf{U} is measured coherently. To accomplish this, a phase pattern is set on the SLM to couple light into the MMF (ideally with low coupling loss). The electric field entering the proximal end of

the MMF for this phase pattern is then measured coherently using the reference beam for both x - and y -polarizations, mathematically decomposed into the basis of forward-propagating fiber modes $\{\bar{\mathbf{E}}_i(x, y, z) | i \in \mathbb{N}, i \leq N\}$, and the resulting vector of mode amplitudes \mathbf{a} stored in the first column of a $N \times N$ matrix denoted by \mathbf{M}_{in} . The z -polarization need not be measured. For the same SLM phase pattern, a similar procedure is followed to measure the electric field exiting the distal end of the MMF through the reflector to obtain \mathbf{b} , which is stored in the first column of a $2P \times N$ matrix denoted by \mathbf{M}_{out} . The relation between \mathbf{a} and \mathbf{b} is given by Eq. (6). This process is repeated N times for N sufficiently different phase patterns, completing measurement of \mathbf{M}_{in} and \mathbf{M}_{out} . Using Eq. (6), these matrices are related by:

$$\mathbf{M}_{\text{out}} = \mathbf{T}\mathbf{U}\mathbf{M}_{\text{in}} \quad (8)$$

$$\mathbf{T}^{-1}(\mathbf{M}_{\text{out}}\mathbf{M}_{\text{in}}^{-1}) = \mathbf{U}, \quad (9)$$

where \mathbf{T}^{-1} is the left inverse of \mathbf{T} , and we require that \mathbf{T} is full rank. This constraint on the reflector makes sense intuitively, as we cannot recover \mathbf{U} if for example there are modes that cannot pass through the reflector. We use ‘‘sufficiently different’’ to mean that the resulting \mathbf{M}_{in} is full rank. It is also possible to perform this procedure using more than N phase patterns, in which case $\mathbf{M}_{\text{in}}^{-1}$ is the right inverse of \mathbf{M}_{in} ; if the data is inconsistent, Eq. (9) gives a least-squares fit for \mathbf{U} .

3.3 Proximal calibration procedure

After distal calibration, whenever the MMF is bent, proximal calibration is performed to measure the resulting perturbed matrix \mathbf{U}_p (with the subscript p on all matrices indicating measurements of a perturbed MMF). The apparatus is configured as in Fig. 2(b), but with beam stop S4 closed, and the same set of N electric fields as in distal calibration are input into the MMF using the same procedure, with the matrix $(\mathbf{M}_{\text{in}})_p$ measured in the same manner. $(\mathbf{M}_{\text{out}})_p$ is measured differently in that it is measured at the proximal end instead of the distal end, and the N electric fields are stored as an $N \times N$ matrix in the basis of backward-propagating fiber modes. The procedure described below is then used to find \mathbf{U}_p . For convenience, we first define matrices \mathbf{Q} and \mathbf{Q}_p :

$$\mathbf{Q} \equiv \mathbf{U}^T \mathbf{R} \mathbf{U} \quad (10)$$

$$\mathbf{Q}_p \equiv \mathbf{U}_p^T \mathbf{R} \mathbf{U}_p, \quad (11)$$

where \mathbf{Q} is known from distal calibration and \mathbf{Q}_p can be calculated using $(\mathbf{M}_{\text{in}})_p$ and $(\mathbf{M}_{\text{out}})_p$:

$$\mathbf{Q}_p = \frac{1}{2}(\mathbf{M}_{\text{out}})_p(\mathbf{M}_{\text{in}})_p^{-1} + \frac{1}{2}((\mathbf{M}_{\text{out}})_p(\mathbf{M}_{\text{in}})_p^{-1})^T. \quad (12)$$

Mathematically, the problem is to solve Eq. (11) for the remaining unknown \mathbf{U}_p when \mathbf{Q}_p and \mathbf{R} are known. To do this, we first perform a Takagi factorization on the matrix \mathbf{Q}_p :

$$\mathbf{Q}_p = \mathbf{V}_p^T \mathbf{D}_q \mathbf{V}_p. \quad (13)$$

This factorization is valid for a complex, square and symmetric matrix; \mathbf{D}_q is real and diagonal and \mathbf{V}_p is complex and unitary. We then perform a Takagi factorization on the matrix \mathbf{R} , which is symmetric for a reflector with symmetric electric and magnetic tensors, as a consequence of reciprocity:

$$\mathbf{R} = \mathbf{W}^T \mathbf{D}_r \mathbf{W}. \quad (14)$$

When Eq. (14) is combined with Eq. (11), this results in

$$\mathbf{Q}_p = \mathbf{U}_p^T \mathbf{W}^T \mathbf{D}_r \mathbf{W} \mathbf{U}_p. \quad (15)$$

By comparing Eqs. (13) and (15), it is apparent that if the Takagi factorization is unique, then

$$\sqrt{\mathbf{D}_r} \mathbf{W} \mathbf{U}_p = \mathbf{N} \sqrt{\mathbf{D}_q} \mathbf{V}_p, \quad (16)$$

where \mathbf{N} is an unknown $N \times N$ diagonal matrix with entries that are ± 1 . Unfortunately, the presence of \mathbf{N} indicates that the solution for \mathbf{U}_p is not unique: there are 2^N possible choices for \mathbf{N} , corresponding to the possible combinations of ± 1 . Aside from \mathbf{N} , the Takagi factorization is unique if \mathbf{U}_p is unitary and the matrix \mathbf{D}_r has unique values [23].

The unknown \mathbf{N} can be found if an estimate is available for the matrix \mathbf{U}_p , namely \mathbf{U} . \mathbf{U} and \mathbf{U}_p satisfy

$$\sqrt{\mathbf{D}_r} \mathbf{W} \mathbf{U}_p = \mathbf{N}_p \sqrt{\mathbf{D}_q} \mathbf{V}_p \quad (17)$$

$$\sqrt{\mathbf{D}_r} \mathbf{W} \mathbf{U} = \mathbf{N} \sqrt{\mathbf{D}_q} \mathbf{V}. \quad (18)$$

If the perturbation is small enough, each row vector from the left-hand side of Eq. (18) can be expected to point in approximately the same direction in $2N$ -dimensional space as the corresponding row vector of Eq. (17). If we orient the pairs of corresponding row vectors in the right-hand sides of Eqs. (17) and (18) in the same manner, then $\mathbf{N} = \mathbf{N}_p$. Thus, \mathbf{U}_p can be recovered without the sign ambiguity by

$$\mathbf{U}_p = \mathbf{W}^\dagger \sqrt{\mathbf{D}_r^{-1}} \mathbf{N} \sqrt{\mathbf{D}_q} \mathbf{V}_p \quad (19)$$

$$\mathbf{N}_{ii} = \text{sgn} \left[\text{Re} \left(\mathbf{v}_{pi}^\dagger \mathbf{v}_i \right) \right], \quad (20)$$

where \mathbf{v}_{pi}^\dagger is the conjugated i th row of \mathbf{V}_p , \mathbf{v}_i is the i th row of \mathbf{V} as a column vector, and sgn denotes the sign function. From this, we conclude that for accurate measurement of \mathbf{U}_p , any perturbation of the MMF must be kept to below an amount that would change the direction of any row vector in Eq. (18) by more than 90° in $2N$ -dimensional space. As will be seen in Section 5, fairly large perturbations can be made while still satisfying this constraint.

To summarize, \mathbf{U}_p can be found using Eq. (19), with terms provided by Eqs. (12), (13), (14), and (20).

3.4 Partial reflector design

The conditions that \mathbf{D}_r must have unique entries and that \mathbf{T} be full rank set two constraints on the design of the partial reflector at the distal end of the MMF. In the noiseless case, these constraints are easy to satisfy; for example, a checkerboard of squares inscribed in the area of the MMF core with alternating high and low reflectance values would suffice. However, noise may make it difficult to distinguish the values of \mathbf{D}_r , and thus it is desirable that individual values be approximately evenly spaced in magnitude. A similar requirement holds for \mathbf{T} , though this is less crucial, since more time is available to reduce noise during distal calibration as compared to proximal calibration. To satisfy both constraints, it is sufficient to have a reflector with approximately as many features as the number of fiber modes per polarization or, equivalently, half the total number of modes. An exemplary reflector design is based on a random grid pattern, and the corresponding values of \mathbf{D}_r are shown in Fig. 3. As can be seen, for the random grid reflector, the entries of \mathbf{D}_r are well-spaced, although the spacings are not perfectly uniform (which would correspond to a linear graph). Typically, the lower-magnitude entries of \mathbf{D}_r correspond to higher spatial frequencies of the reflector, and tend to increase in magnitude as the number of spatial features increases.

A possible realization of the reflector shown is as follows. Assume the MMF core refractive index is 1.473 and the medium outside is water, whose index is 1.333. Each square is a single-layer reflector with refractive index of 2.43 and thickness between 109 and 166 nm, sampled from a uniform probability distribution. The reflectance and transmittance values specified in Fig. 3 are from a higher-index medium to a lower-index medium, so transmittance values with magnitude exceeding unity are permissible. The individual squares have dimensions of about $2 \mu\text{m} \times 2 \mu\text{m}$, which may be patterned using photolithography [24]. Care must be taken to ensure that any possible gaps between the reflector and the MMF accidentally created during the fabrication process are thin compared to the reflector thickness.

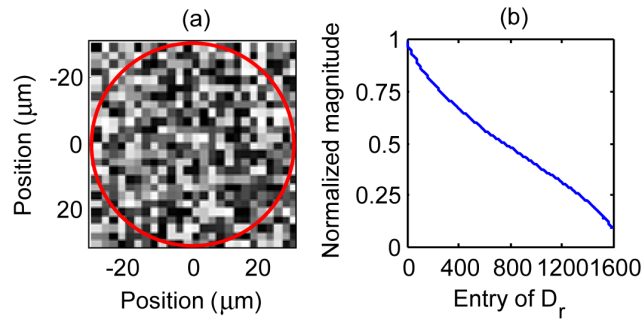


Fig. 3. (a) Electric field amplitude reflectance and transmittance values of partial reflector. The red circle indicates the MMF core. Reflectance is indicated by image brightness; black represents an amplitude reflectance and transmittance of 0.05 and 1.05, respectively, while white represents an amplitude reflectance and transmittance of 0.50 and 0.91, respectively. (b) Entries of the matrix (\mathbf{D}_r), for an MMF with 1588 modes.

Of potential concern is the physical precision of the reflector created by this fabrication process. While small deviations from the design specifications will not adversely affect the function of the reflector due to the high degree of freedom available for the reflector design, the reflector as fabricated must be measured accurately. As these measurements will necessarily have some error, it would be reassuring to know what impact the measurement error may have on the accuracy of proximal calibration. This impact is discussed and shown in Fig. 4 below.

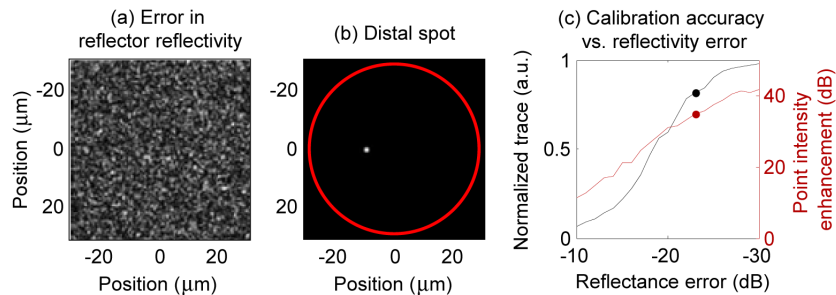


Fig. 4. Accuracy of proximal calibration with errors in the measurement of the partial reflector. The error in the reflector is shown in (a) for a reflectance error of -23 dB , where reflectance error is characterized by the standard deviation of the error in the measured reflectance divided by the mean reflectance. The intensity pattern of a distal spot at -23 dB error is shown in (b). Calibration accuracy is plotted in (c) for errors ranging from -10 to -30 dB (10% to 0.1%); accuracy is characterized both by the trace divided by the number of rows of the matrix $(\mathbf{U}_p)_{\text{actual}}(\mathbf{U}_p)_{\text{calc}}^{-1}$, as plotted in black on the left axis, and by the ratio of spot peak intensity divided by mean background intensity, as plotted in red on the right axis. The points corresponding to an error of -23 dB are indicated.

When there is an error in the measurement of the reflectance of the reflector, an incorrect \mathbf{R} will be used in Eqs. (10)-(20), which results in an incorrect \mathbf{U}_p . Thus, the calculated $(\mathbf{U}_p)_{\text{calc}}$ will be different from the actual $(\mathbf{U}_p)_{\text{actual}}$. The accuracy of $(\mathbf{U}_p)_{\text{calc}}$ can be characterized by how close $(\mathbf{U}_p)_{\text{actual}}(\mathbf{U}_p)_{\text{calc}}^{-1}$ is to the identity matrix, since $(\mathbf{U}_p)_{\text{calc}}$ is used to invert $(\mathbf{U}_p)_{\text{actual}}$; alternatively, it can also be characterized by the quality of a spot generated at the distal end of the MMF using $(\mathbf{U}_p)_{\text{calc}}$ employing a procedure described in the following section. The relation between calibration accuracy and reflector error is illustrated in Fig. 4. Figure 4(a) shows the absolute value of the difference between the measured and actual reflectances of the reflector for a reflectance error (the standard deviation of the error in the reflectance divided by the mean reflectance) of -23 dB. Figure 4(b) shows a corresponding spot formed at the distal end of the MMF when using $(\mathbf{U}_p)_{\text{calc}}$. Figure 4(c) plots the trace divided by the number of rows of the matrix $(\mathbf{U}_p)_{\text{actual}}(\mathbf{U}_p)_{\text{calc}}^{-1}$, on the left axis, and the spot peak intensity divided by mean background intensity, on the right axis, versus reflectance errors ranging from -10 to -30 dB. It can be seen that good results can be obtained with reflectance errors of -23 dB (0.5%) or less, though the tolerable value will change depending on the number of modes of the MMF. Thus, although the reflector must be measured with high accuracy, small measurement errors are not catastrophic for the technique.

4. Imaging procedure

After calibration, when \mathbf{U}_p is known, the procedure for forming a spot in an object plane parallel to and outside the distal facet of the MMF can be achieved by exciting the input electric field at the proximal end according to:

$$\mathbf{s}_{\text{in}} \equiv \mathbf{M}^\dagger \mathbf{U}_p^\dagger (\mathbf{FT})^{-1} \hat{\mathbf{e}} \quad (21)$$

$$\mathbf{s}_{\text{out}} = \mathbf{FTU}_p \mathbf{M} \mathbf{s}_{\text{in}}, \quad (22)$$

where the inverse of \mathbf{FT} is the left inverse; \mathbf{M} is an $N \times 2P$ matrix whose rows are the conjugated electric fields $\vec{\mathbf{E}}^*(x, y)$ of each forward-propagating mode (discretized in the same manner as \mathbf{T}); \mathbf{F} is a $2P \times 2P$ convolution matrix that performs free space propagation from the distal MMF facet to the object plane, implemented here using Rayleigh-Sommerfeld diffraction theory [25]; \mathbf{s}_{in} is the $2P \times 1$ input electric field at the proximal end of the MMF; \mathbf{s}_{out} is the resulting $2P \times 1$ output electric field in the object plane, and $\hat{\mathbf{e}}$ is a $2P \times 1$ standard basis vector with one nonzero entry corresponding to the location and polarization of the desired spot in the parallel plane. Note that we have used the approximation that the electric field vanishes in the z polarization; for each mode of the fiber considered here, the z polarization holds approximately 1% of the total power, so this approximation is satisfied sufficiently well for imaging. Equations (21)-(22) compute the input vector \mathbf{s}_{in} that minimizes the l^2 norm between \mathbf{s}_{out} and $\hat{\mathbf{e}}$, so that \mathbf{s}_{out} is a spot at the location of $\hat{\mathbf{e}}$ and in the same polarization. By changing \mathbf{F} , spots can be formed on a plane at a different distance from the distal MMF facet.

For imaging, the apparatus is configured as in Fig. 2(b), with the only difference from calibration being that the shutter (beam stop S4) is open and light can enter the MMF. The electric field measured at the proximal end of the MMF due to the reflection of a spot from the object is then given by:

$$\mathbf{s}_{\text{meas}} = \mathbf{M}^\dagger \mathbf{U}_p^\dagger (\mathbf{T}^\dagger \mathbf{F} \mathbf{s}_{\text{refl}} + \mathbf{R} \mathbf{U}_p \mathbf{M} \mathbf{s}_{\text{in}}), \quad (23)$$

where \mathbf{s}_{refl} is the electric field reflected from the object. We have assumed that the object is thin and there are no other sources of reflection between the distal MMF facet and the object plane [25]. To perform image reconstruction, we first subtract off the light reflected inside the MMF from the reflector:

$$\mathbf{s}_{\text{sub}} = \mathbf{s}_{\text{meas}} - \mathbf{M}^T \mathbf{U}_p^T \mathbf{R} \mathbf{U}_p \mathbf{M} \mathbf{s}_{\text{in}}. \quad (24)$$

We then invert the distortion caused by transmission through the reflector:

$$\mathbf{s}_{\text{fin}} = (\mathbf{T}^T \mathbf{F})^{-1} \mathbf{U}_p^* \mathbf{M}^* \mathbf{s}_{\text{sub}}. \quad (25)$$

where the inverse of $\mathbf{T}^T \mathbf{F}$ is the right inverse. Finally, the total power of the reflected spot is found by performing a normalization:

$$p = \frac{\|\mathbf{s}_{\text{fin}}\|^2}{\|\mathbf{s}_{\text{unif}}\|^2}, \quad (26)$$

where $\|\mathbf{s}_{\text{unif}}\|^2$ is the total power expected for reflection of the spot from a perfect mirror object. This normalization ensures that the image brightness does not decrease away from the center of the MMF core. \mathbf{s}_{unif} can be computed or measured experimentally, and does not depend on \mathbf{U} . The final expression for p is then the normalized power of \mathbf{s}_{refl} , which is an approximation of the reflectance of the object at the location of $\hat{\mathbf{e}}$. By sequentially creating spots at all possible $\hat{\mathbf{e}}$, and assigning each p to the location of the corresponding spot, an image of the intensity reflectance of the object is formed.

5. Simulation of imaging

In this section, we describe simulation of the MMF endoscope shown in Fig. 2. The unperturbed mode coupling matrix \mathbf{U} is modeled as a Haar-distributed random unitary matrix [26]. To model perturbation from fiber bending, the perturbed mode coupling matrix is computed as $\mathbf{U}_p = \mathbf{P}\mathbf{U}$, where $\mathbf{P} \equiv e^{i\mathbf{H}}$, \mathbf{H} is a random Hermitian matrix and k is a positive real number. By construction, \mathbf{P} is a random unitary matrix. By increasing k , the strength of the bending-induced perturbation may be scaled up. The reflector attached to the distal end of the MMF is the same as that shown in Fig. 3, and the MMF is assumed to be immersed in water. Noise is neglected. The mode coupling matrix of the MMF is measured using the procedure described in Section 3, and spots are formed in an object plane 50 μm from the distal end of the MMF.

Figure 5 compares spots formed through a fiber that has been calibrated at the distal end, then perturbed by bending. In Fig. 5(a), a subsequent proximal calibration is not performed, so the unperturbed mode coupling matrix \mathbf{U} is employed to compute the input electric field distribution, and a high-quality spot is not obtained. In Fig. 5(b), a subsequent proximal calibration is performed, so the perturbed mode coupling matrix \mathbf{U}_p is employed in computing the input field distribution, and a well-localized spot is obtained. Simulations show that even when the perturbation \mathbf{P} is so strong that the spot disappears when the unperturbed \mathbf{U} is used in computing the input field distribution, \mathbf{U} remains a sufficiently accurate estimate of \mathbf{U}_p to enable successful proximal calibration and formation of well-localized spots.

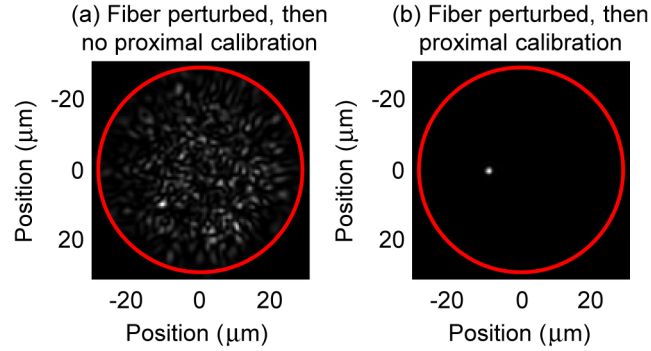


Fig. 5. Formation of a spot through a fiber that has been perturbed after distal calibration. (a) Spot formed with an input electric field computed using (\mathbf{U}) , the unperturbed mode coupling matrix. (b) Spot formed with an input electric field computed using $(\mathbf{U})_p$, the perturbed mode coupling matrix measured using proximal calibration.

After distal calibration, a specular reflective object is imaged. The object is located in the object plane $50 \mu\text{m}$ from the distal fiber facet, and has the reflectance shown in Fig. 6(a). A grid of spots spaced $0.31 \mu\text{m}$ apart is sequentially excited on the object plane using the procedure described in Section 4, and an image is reconstructed from the reflected powers. Two reconstructed images are shown in Fig. 6(b) and 6(c). Figure 6(b) represents an image obtained using a rigid MMF endoscope [27], to provide a reference for evaluating the flexible MMF endoscope. To obtain Fig. 6(b), distal calibration is performed without a reflector on the distal fiber end to obtain the unperturbed mode coupling matrix \mathbf{U} , the fiber remains unperturbed, and imaging is performed using \mathbf{U} . Figure 6(c) represents an image obtained using the flexible MMF endoscope described here. After distal calibration through the reflector on the distal fiber end, the fiber is perturbed by a random unitary matrix \mathbf{P} , proximal calibration is performed to obtain the perturbed mode coupling matrix \mathbf{U}_p , and imaging is performed using \mathbf{U}_p .

In Fig. 6, there is no apparent decrease in image quality between the rigid endoscope (Fig. 6(b)) and the flexible endoscope (Fig. 6(c)), even though the latter relies on proximal-end calibration and images through the reflector. In theory the reflector decreases the amount of light that re-enters the MMF and causes the point-spread function of the imaging system to not be spatially invariant, but in this example the effects are negligible. This is true for the reflector design shown in Fig. 3, but is not true in general. For example, a reflector with very high spatial frequencies will cause artifacts in the recorded image.

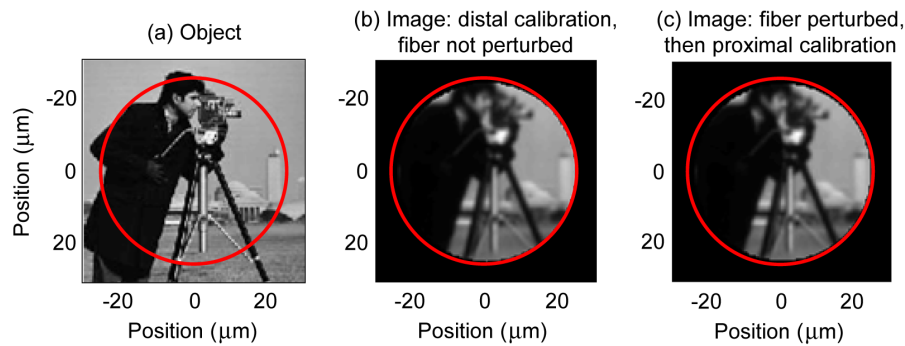


Fig. 6. (a) Cameraman object. (b) Image formed through a fiber that has not been perturbed after distal calibration, using the unperturbed matrix (\mathbf{U}) . (c) Image formed through a fiber that has been perturbed after distal calibration, using the perturbed matrix $(\mathbf{U})_p$ measured using proximal calibration.

6. Discussion

We anticipate two challenges to performing the proximal calibration procedure in practice. The first challenge relates to the continuous calibration required as the endoscope is maneuvered to the target site, during which, bending of the fiber continually changes the perturbed transmission matrix \mathbf{U}_p . The time required to measure \mathbf{U}_p must be sufficiently short that the current estimate of \mathbf{U}_p always remains sufficiently accurate to enable correct determination of an updated estimate of \mathbf{U}_p . In practice, calibration time is usually limited by the frame rate of the SLM. Methods for speeding up calibration have been described [4,5]. Note that calibration time scales linearly in proportion to the number of modes guided by the MMF (assuming that data processing speed is not a bottleneck). The second challenge relates to degradation of the calibration by noise. Care must be exercised to ensure that the entries of the reflector factorization matrix \mathbf{D}_r are distinguishable and are measured accurately, which means that the SNR must increase in proportion to the number of modes guided by the MMF. Both challenges may be addressed by using an MMF supporting fewer modes, but at the expense of reduced imaging resolution.

In the proximal calibration procedure described above, the matrices \mathbf{U} and \mathbf{U}_p are assumed to be unitary, i.e., the MMF is assumed lossless. Although this is a good approximation, even a short fiber has some amount of loss and, as mentioned in Section 4, a non-unitary matrix will result in an incorrect solution for \mathbf{U} . Fortunately, the solution for \mathbf{U} converges uniformly to the correct one as \mathbf{U} approaches a unitary matrix, and losses are sufficiently low that non-unitarity is not expected to be an issue in practice.

In Section 3, the reflectance matrix \mathbf{R} of the reflector is assumed symmetric as a consequence of reciprocity. If \mathbf{R} is not symmetric, \mathbf{Q}_p is no longer symmetric and the singular value decomposition (SVD) can be used instead of the Takagi factorization. In this case, Eqs. (13) and (15) are replaced by:

$$\mathbf{Q}_p = \mathbf{V}_p^T \mathbf{D}_q \mathbf{X}_p \quad (27)$$

$$\mathbf{Q}_p = \mathbf{U}_p^T \mathbf{W}^T \mathbf{D}_r \mathbf{Y} \mathbf{U}_p. \quad (28)$$

As a consequence, there are now two different unitary matrices appearing on either side of both \mathbf{D}_q and \mathbf{D}_r , which is necessary for the decomposition of non-symmetric matrices. Like the Takagi factorization, the SVD is unique under the same conditions. When Eqs. (27) and (28) are compared, there are then two equations to be solved to find \mathbf{U}_p , instead of one as in the symmetric case:

$$\mathbf{V}_p^T \mathbf{N}^* = \mathbf{U}_p^T \mathbf{W}^T \quad (29)$$

$$\mathbf{N} \mathbf{X}_p = \mathbf{Y} \mathbf{U}_p. \quad (30)$$

It is then possible to simultaneously solve Eqs. (29) and (30) and thereby resolve the ambiguity due to the diagonal matrix \mathbf{N} , which allows \mathbf{U}_p to be measured without requiring a prior approximation for \mathbf{U}_p . This is not taken advantage of in the design of the endoscope and calibration procedures, as it is expected to be difficult to fabricate a reflector with a substantially non-symmetric \mathbf{R} .

Finally, we note that it is not strictly necessary to excite a spot in both polarizations at the object plane unless the object is expected to be strongly birefringent. Thus, one might expect that calibration time could be cut in half by ignoring polarization. However, when the procedure to form a spot is then attempted, the excited fields will be randomly split between the two polarizations, making it impossible to ensure that a localized spot is formed. Correctly exciting only one polarization would then require a linear polarizer to be placed before the

reflector. This is not incorporated in the endoscope design, as it would complicate fabrication of the reflector.

7. Conclusion

Although significant progress has been made in the development of MMF endoscopes, the requirement for distal-end calibration has forced all endoscope designs to date to be rigid. In this paper, we described a design for an MMF endoscope that can be bent while it is maneuvered to the target imaging site. This is achieved by attaching a partial reflector to the distal end of the MMF, which allows the MMF to be calibrated even while it is being maneuvered. Three requirements for this procedure to work are (a) the MMF must be recalibrated each time the MMF is bent; (b) a shutter must be present at the distal end of the MMF; and (c) the reflectance and transmittance of the partial reflector at the distal end must be known. From simulations of proximal calibration and subsequent imaging through an MMF with 1588 modes, we found that proximal calibration works even for substantial perturbation of the MMF, and the quality of images recorded through the partial reflector after proximal-end calibration are comparable to those obtained using a rigid endoscope without a partial reflector using distal-end calibration.